AFRL-AFOSR-VA-TR-2019-0067

Fundamental Turbulence Mechanisms in Multi-Stream Flows: A Comprehensive Joint Experimental, Theoretical and Computational Study

Mark Glauser
SYRACUSE UNIVERSITY
CONTROLLERS OFFICE SKYTOP OFFICE BLD
SYRACUSE, NY 13244

03/28/2019
Final Report

DISTRIBUTION A: Distribution approved for public release.

Air Force Research Laboratory
AF Office Of Scientific Research (AFOSR)/RTA1
Arlington, Virginia 22203
Air Force Materiel Command

REPORT DOCUMENTATION PAGE

Form Approved
OMB No. 0704-0188

1. REPORT DATE *(DD-MM-YYYY)*	2. REPORT TYPE	3. DATES COVERED *(From - To)*
28-03-2019	Final Performance	28 Sep 2015 to 27 Sep 2018

4. TITLE AND SUBTITLE
Fundamental Turbulence Mechanisms in Multi-Stream Flows: A Comprehensive Joint Experimental, Theoretical and Computational Study

5a. CONTRACT NUMBER

5b. GRANT NUMBER
FA9550-15-1-0435

5c. PROGRAM ELEMENT NUMBER
61102F

6. AUTHOR(S)
Mark Glauser, Jacques Lewalle

5d. PROJECT NUMBER

5e. TASK NUMBER

5f. WORK UNIT NUMBER

7. PERFORMING ORGANIZATION NAME(S) AND ADDRESS(ES)
SYRACUSE UNIVERSITY
CONTROLLERS OFFICE SKYTOP OFFICE BLD
SYRACUSE, NY 13244 US

8. PERFORMING ORGANIZATION REPORT NUMBER

9. SPONSORING/MONITORING AGENCY NAME(S) AND ADDRESS(ES)
AF Office of Scientific Research
875 N. Randolph St. Room 3112
Arlington, VA 22203

10. SPONSOR/MONITOR'S ACRONYM(S)
AFRL/AFOSR RTA1

11. SPONSOR/MONITOR'S REPORT NUMBER(S)
AFRL-AFOSR-VA-TR-2019-0067

12. DISTRIBUTION/AVAILABILITY STATEMENT
A DISTRIBUTION UNLIMITED: PB Public Release

13. SUPPLEMENTARY NOTES

14. ABSTRACT
In this effort we deployed, to a multi-stream Single Expansion Rectangular Nozzle (SERN), the latest advances in simulations, experimental methods and analysis tools denoted the Fluids Information Triad (FIT) in a tightly integrated manner that fuses their respective strengths. Our interest in the multi-stream SERN is distilled from the fact that such a configuration is of intense current interest to the USAF, as it seeks new exhaust systems that maximize efficiency and performance of future aircraft. We have demonstrated the effectiveness of the FIT approach through the integration of experiments and simulations. The experiments have brought to bear high-fidelity diagnostics, while the simulations have employed Large-Eddy Simulations. In this study we have focused on validation, data fusion and flow physics. Substantial effort has been expended on establishing the accuracy of these results through detailed two-way validation exercises. We have found excellent comparison for example between mean planar PIV with averaged Large-Eddy Simulation (LES) data, pointwise comparison of the evolution of the shear layer downstream of the deck as well as instantaneous measured and simulated Schlieren images. These and other results in like vein clearly establish the realism of our data acquisition and generation techniques.

15. SUBJECT TERMS
Turbulence, Single Expansion Ramp Nozzles (SERN), Multi-stream nozzle flow

16. SECURITY CLASSIFICATION OF:			17. LIMITATION OF ABSTRACT	18. NUMBER OF PAGES	19a. NAME OF RESPONSIBLE PERSON
a. REPORT	b. ABSTRACT	c. THIS PAGE			SMITH, DOUGLAS
Unclassified	Unclassified	Unclassified	UU		

Standard Form 298 (Rev. 8/98)
Prescribed by ANSI Std. Z39.18

				19b. TELEPHONE NUMBER *(Include area code)* 314-235-6013

Final Report: Fundamental Turbulence Mechanisms in Multi-Stream Flows A Comprehensive Joint Experimental, Theoretical andComputational Study

AFOSR Grant Number FA9550-15-1-0435
9/28/2015 - 9/27/2018

Mark Glauser and Jacques Lewalle
Syracuse University, Syracuse New York 13244
and

Datta V. Gaitonde
The Ohio State University, Columbus, Ohio 43210

Abstract

In this effort we deployed, to a multi-stream Single Expansion Rectangular Nozzle (SERN), the latest advances in simulations, experimental methods and analysis tools – denoted the Fluids Information Triad (FIT) in a tightly integrated manner that fuses their respective strengths. Our interest in the multi-stream SERN is distilled from the fact that such a configuration is of intense current interest to the USAF, as it seeks new exhaust systems that maximize efficiency and performance of future aircraft. We have demonstrated the effectiveness of the FIT approach through the integration of experiments and simulations. The experiments have brought to bear high-fidelity diagnostics, while the simulations have employed Large-Eddy Simulations. In this study we have focused on validation, data fusion and flow physics. Substantial effort has been expended on establishing the accuracy of these results through detailed two-way validation exercises. We have found excellent comparison for example between mean planar PIV with averaged Large-Eddy Simulation (LES) data, pointwise comparison of the evolution of the shear layer downstream of the deck as well as instantaneous measured and simulated Schlieren images. These and other results in like vein clearly establish the realism of our data acquisition and generation techniques.

1. Numerical and Experimental Methodology

Numerical Methodology

The computational campaign was performed in tight coordination with the experiments. Large-Eddy Simulations (LES) were performed by solving the 3-D compressible Navier-Stokes equations in non-dimensional, curvilinear coordinates (Vinokur 1974) using a structured finite-difference solver (Gaitonde & Visbal 1998; Stack & Gaitonde 2018; Visbal & Gaitonde 1997, 2001). Numerous simulations were performed at the full Reynolds number of the experiment, corresponding to $Re \sim 2.70 \times 10^6$, based on nozzle exit conditions attained from isentropic relations at the design Mach number of 1.6, and the hydraulic diameter. The LES procedure followed the general approach of Grinstein *et al.* (2007), with care being exercised to ensure the results of interest were insensitive to grid resolution. Inviscid fluxes were evaluated with a third-order upwind-biased Roe scheme (Roe 1981) using van Leer's harmonic limiter (van Leer 1979) to minimize numerical diffusion, provide sub-grid closure, and mitigate unphysical oscillations in the vicinity of discontinuities. Viscous fluxes were evaluated with centered, second-order derivatives. For time-integration, we utilized an implicit approach based on the Beam-Warming method (Beam & Warming 1978) with a sub-iteration scheme to address errors associated with explicitly-specified boundary conditions, flux linearization, and approximate factorization. In the present case, we found a time step size of approximately $\Delta t = 47ns$, coupled with two sub- iterations, provided consistent results. Previous simulations with the same approach, including numerous comparisons with experiments, may be found in Gaitonde & Samimy (2011); Gonzalez *et al.* (2016); Speth & Gaitonde (2015).

To ensure solution consistency, the calculation was repeated on grids containing $176M$ (designated "nominal"), $300M$ ("intermediate"), and $600M$ ("fine") nodes respectively (where "M" denotes million). The streamwise and transverse grid topologies were consistent between all of the grids, with an example shown in Figs. 1a and 1b. All grids were highly refined in the streamwise direction near the nozzle lip and aft-deck trailing edge, and spread in the transverse and spanwise directions downstream of the nozzle exit to account for plume deflection and shear layer growth (Figs. 1b and 1c). The spreading and deflection angles of the grids were guided both by experimental results and preliminary simulations (not described here). The nominal grid was designed to ensure adequate support for shear layers based on prior experience, as well as to obtain the correct shock positions, with a gradual drop off in resolution downstream of the deck. The intermediate mesh was obtained through refinement of the downstream plume region, while the fine grid emphasized resolution in the shear layers to better resolve turbulent structures, as well as boundary layers through tighter wall-normal spacings.

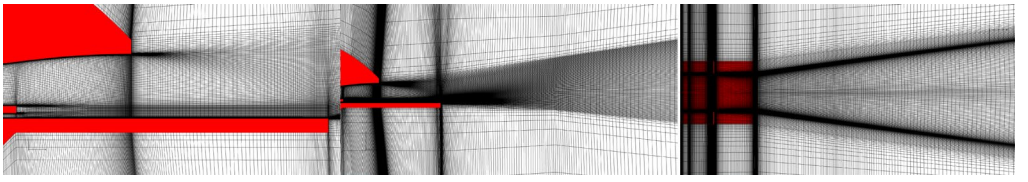

(a) Near-nozzle symmetry plane. (b) Full symmetry plane. (c) Spanwise plane.

Figure 1: **Mesh point distribution features. Every fourth node is shown for clarity, and the nozzle geometry is colored in red.**

Outside the nozzle components, a small co-flow of $6m/s$ was specified as in the corresponding experiments. The inflow within the nozzle was specified as described below. All walls were assumed to be adiabatic, and the no-slip condition is enforced. Regarding the far-field boundary conditions, due to the combination of the distance from the configuration, the grid stretching near the boundaries, and the dissipative nature of the upwind scheme, the implementation of the zero-gradient condition did not produce any noticable reflections. For each grid, statistical stationarity was ensured prior to sampling for statistical analyses.

The inflow conditions are a critical component in the accurate simulation of nozzle flows, as the properties of the boundary layer exiting the nozzle are known to have a substantial effect on the downstream evolution of jet plumes (Bogey & Bailly 2010; Speth & Gaitonde 2012; Zaman 2012). For example, Bogey & Bailly (2010) showed through numerical simulations that the addition of a small amount of inlet noise led to weaker vortex pairing events, an increase in potential core length, and a reduction of far-field sound pressure levels. Thus, high-fidelity simulations clearly require special care in the specification of these conditions.

Since the LES could not extended to the internal nozzle flow because of prohibitive computational requirements associated with the simulation of the complex transition processes, we specified an incoming turbulent boundary layer with a synthetic method. A review of several turbulent inflow generation methods, particularly in regards to flat plate, zero pressure-gradient boundary layers, can be found in Dhamankar *et al.* (2014). However, since two independent rectangular streams must be specified in this case, with each exhibiting its own three-dimensional characteristics due to nozzle curvature, and corner effects, a more sophisticated method is needed than those commonly used for flate plate boundary layers. One of the few methods that can account for the three-dimensional complexities associated with practical configurations is digital filtering (Klein *et al.* 2003; Touber & Sandham 2008), which has been primarily used for flat plate boundary layers (Adler & Gaitonde 2017; Touber & Sandham 2008), but has now been generalized in this effort to be applicable to multiple rectangular streams (Adler *et al.* 2018; Stack & Gaitonde 2017, 2018). Briefly, the method generates instantaneous 2-D turbulent inflow planes by combining mean velocity and Reynolds stress distributions with fluctuations derived from filtered random numbers that are correlated in space and time. The mean flow and Reynolds stresses are usually obtained from existing databases derived from DNS or LES data (Touber & Sandham 2008), sometimes at different conditions than those of interest. Since such data are not available for our case, and as noted above, it is not feasible to perform an LES of the internal flow, we extract the pertinent flowfield statistics near the nozzle throat from a separate Reynolds-averaged Navier-Stokes (RANS) simulation. The results of Adler *et al.* (2018) demonstrate that such RANS-based data relaxes relatively quickly to the desired equilibrium turbulent profile.

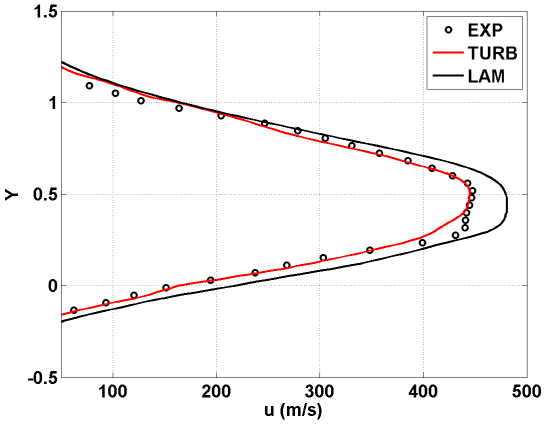

Figure 2: **Comparison of *u*-velocity profiles between PIV measurements, and simulation results with and without a turbulent inflow.**

The necessity of applying this turbulent inflow methodology is displayed in Fig. 2, which compares *u*-velocity profiles from simulations with laminar (black line) and turbulent (red line) inflow conditions, to experimental PIV results (black circles). The profiles are extracted on the nozzle symmetry plane (*x*-*y* plane through the center of the major axis) at a streamwise location of $x/D_h = 4$ (where $x/D_h = 0$ is the nozzle exit, and $x/D_h = 2$ is the aft-deck trailing edge). It is clear that the specification of an incoming turbulent boundary layer is crucial to replicate the shear layer phenomena occurring in the experiment, since the simulation with the turbulent inflow agrees very well with PIV results, while the simulation with laminar conditions does not. The adequacy of this method is further apparent below, where we compare LES results using a turbulent inflow to experimental measurements in a more rigorous fashion.

Experimental Facility and Methodology

The high speed jet facility at Syracuse University, configured with the SERN supersonic nozzle assembly is the key experimental facility for the effort. This facility is capable of core jet Mach numbers up to 1.7 and deck/wall-jet flow Mach numbers from 0 to 1.7. and is housed in a very large anechoic chamber allowing for simultaneous noise measurements. The facility is instrumented with a Dantec Particle Image Velocimetry (PIV) system, extensive high-bandwidth pressure and acoustic sensors, along with several high-speed data acquisition systems for high-bandwidth pressure/acoustic sensor signal acquisition, as well as a high-resolution Schlieren system. All of the instrumentation is configured to be sampled simultaneously allowing for extensive spectra and cross-spectra and unsteady features to be captured as discussed below.

2. Validation

Validation was achieved by comparing mean and instantaneous quantities on different grids to their experimental counterparts acquired at Syracuse University (Berry *et al.* 2016; Magstadt *et al.* 2016). First, the time-averaged symmetry plane *u*-velocity fields are presented to show that all simulations replicate the primary features observed in the experiment. Subsequently, shock positions are compared throughout the plume using both time-averaged and instantaneous Schlieren images. Finally, unsteady content is compared using deck pressure measurements.

Figure 3 shows the time-averaged symmetry plane *u*-velocity fields from the three

different grids (Figs. 3a, 3b, and 3c), and from experimental PIV measurements (Fig. 3d). By comparing the *u*-velocity fields from the simulations to the experiment, it is clear the key attributes of velocity magnitudes, entrainment-driven spreading rates, and upwards plume deflection downstream of the aft-deck closely resemble each other.

A quantitative assessment of the comparison with experimental PIV data is displayed in Fig. 4 using time-averaged symmetry plane *u*-velocity profiles at select downstream locations.

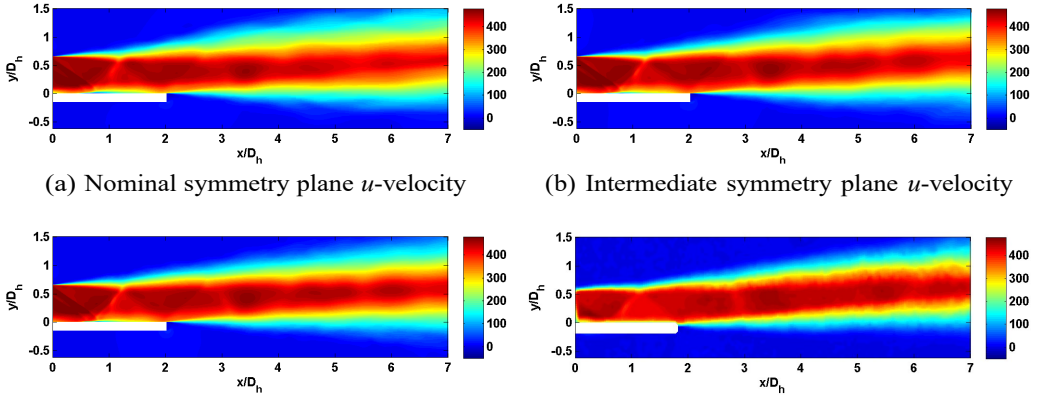

(a) Nominal symmetry plane *u*-velocity (b) Intermediate symmetry plane *u*-velocity

(c) Fine symmetry plane *u*-velocity (d) PIV symmetry plane *v*-velocity

Figure 3: **Comparison of time-averaged symmetry plane *u*-velocity fields between the three grids and the experiment.**

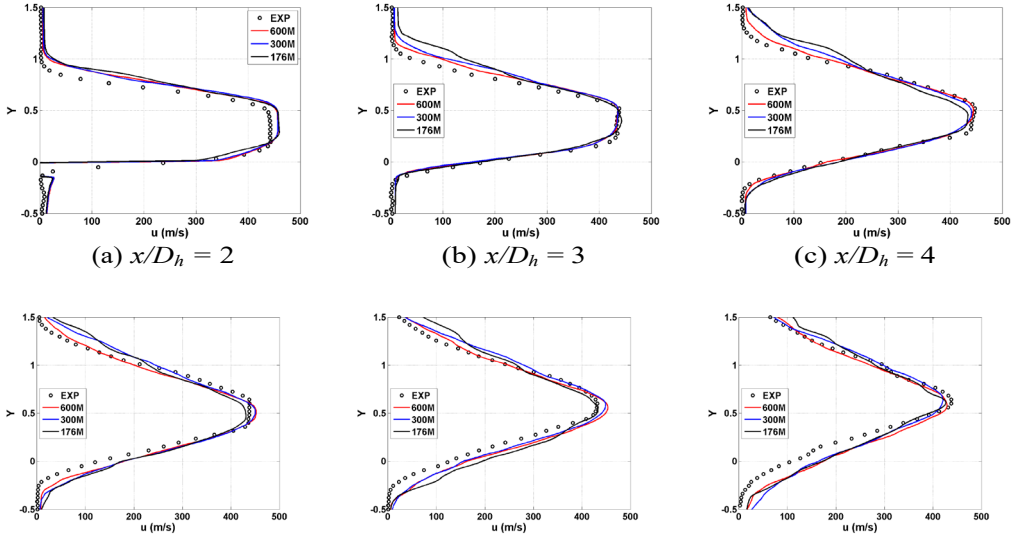

(a) $x/D_h = 2$ (b) $x/D_h = 3$ (c) $x/D_h = 4$

(d) $x/D_h = 5$ (e) $x/D_h = 6$ (f) $x/D_h = 7$

Figure 4: **Comparison of time-averaged symmetry plane *u*-velocity fields at selected axial locations.**

The simulations capture the main features, including the expansions/compressions of the velocity field through the shock train, quite accurately. Likewise, the evolution of the velocity profiles from relatively sharp transverse gradients to more diffuse shear layers is reproduced. The deflection of the plume as it develops downstream is clearly visible in the upward movement of peak velocity values with increasing downstream distance, resulting in an estimated deflection angle of 3.83^o. Additionally, the location where the core and deck streams merge is often of interest, as it determines the location where the secondary flow (deck stream) is no longer effective in reducing Mach wave radiation (Papamoschou & Debiasi 2001).

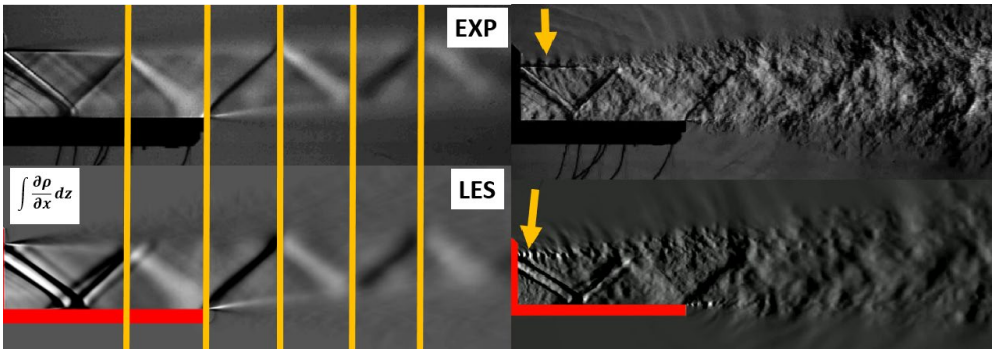

(a) (b)

Figure 5: **Sideline Schlieren of: (a) the time-averaged flow, (b) an instantaneous snapshot. The top images show the experiment (Magstadt *et al.* 2016) and the bottom images show the LES results.**

Figure 4 indicates that the demarcation between the deck and core streams disappears relatively quickly downstream of the deck (before $x/D_h = 3$), partly due to the enhanced mixing associated with the deck boundary layer. Sensitivity to spatial resolution is relatively modest for the chosen mesh densities, and the agreement with experimental data is clearly evident. The experimental measurements exhibit a slightly slower growth rate of the shear layer on the deck side, though some error may be associated with uncertainties in mapping the measurements to physical coordinates.

A comparison of the time-averaged and instantaneous streamwise shock positions is presented in Fig. 5 using the fine grid (unless otherwise noted, all subsequent results are derived from this grid). The numerical Schlieren is generated by integrating the streamwise density gradient across the span of the jet to mimic the measured quantity. The mean positions of the shocks are in good agreement throughout the plume, as evident in Fig. 5a, where shock reflection locations are marked with vertical yellow lines. The instantaneous Schlieren visualizations in Fig. 5b also show considerable similarity between the simulation and experimental data. Signatures of shear layer instabilities and shedding are observed (marked by arrows), which generate disturbances that propagate along the shocks emanating from the upper ramp (Berry *et al.* 2017; Magstadt 2017). The spreading rates of the jets are also comparable, and both figures indicate the presence of fine-scale acoustic features just outside the plume.

To highlight some of the three-dimensional aspects of the shock train, time-averaged and instantaneous top-view Schlieren images are presented in Fig. 6, generated in the same manner as Fig. 5, but with the integration direction being taken in the transverse direction, in accordance with the experimental setup. The time-averaged shock positions of the experiment and LES, shown in Fig. 6a, again exhibit similar features. In addition to the prominent diamond pattern, which results from the side-wall shocks, features oriented normal to the streamwise direction are also visible, as highlighted by arrows. The most

notable such feature occurs just upstream of the interaction of the side-wall shocks, and is the trace of the SERN shocks (Fig. 5). The instantaneous realization of the shock positions in Fig. 6b depicts turbulent fluctuations of density in both experiment and simulations. As with the sideline Schlieren images above, additional details observed in these images will be discussed later.

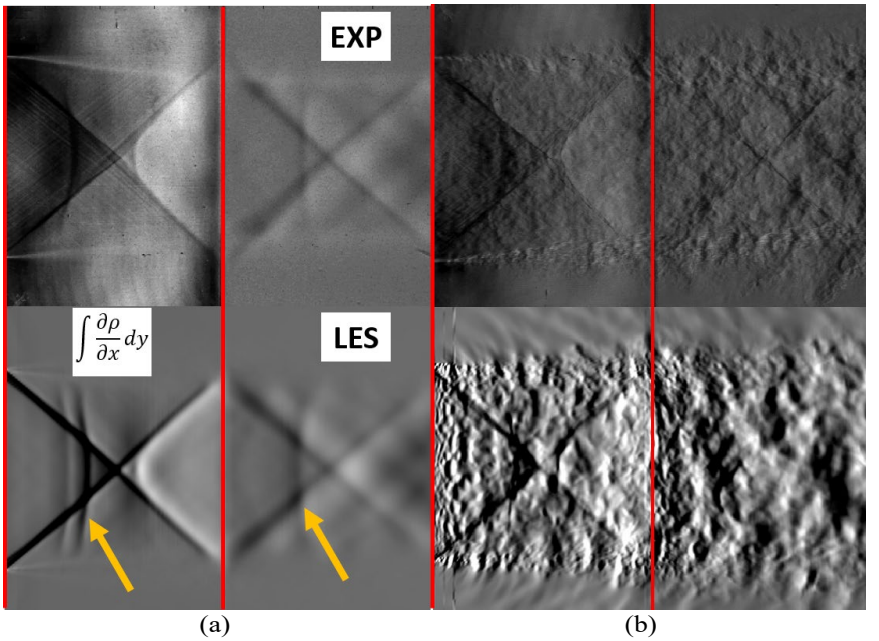

(a) (b)

Figure 6: **Top-views of simulated and measured Schlieren images: (a) time-averaged flow, (b) an instantaneous snapshot. The upper images show the experimental observations (Magstadt *et al.* 2016) and the bottom images show the LES. The left side of the image is the nozzle exit and the red line denotes the end of the deck. Yellow arrows highlight SERN-associated shocks.**

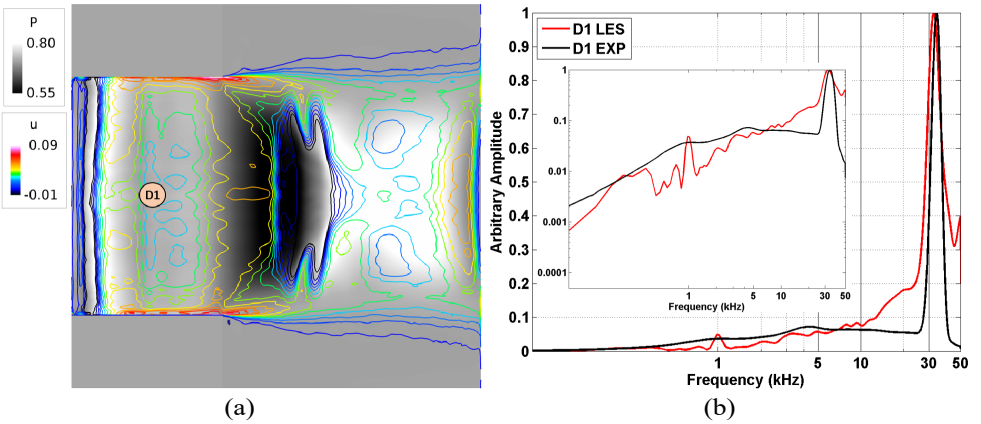

(a) (b)

Figure 7: **Deck pressure: (a) probe location marked on the top-view of the deck, (b) PPSD from samplings at 100*kHz*. The primary plot is on a log-linear scale, and the inset is a log-log scale.**

To compare the unsteady content from simulations to the experiment, deck pressure measurements are utilized at the location shown in Fig. 7a, where the left side of the image is the splitter plate trailing edge, and the right side is the aft-deck trailing edge. For additional reference, this figure also depicts contours of the time-averaged u-velocity, and grey scale values of the pressure one node above the deck surface, the former being a simple surrogate for the wall shear stress. The spatial variation of the pressure results from the influence of the shock train on the deck, which is related to the upwards plume deflection, and flow separation, both of which are further examined later. The premultiplied Power Spectral Density (PPSD) of the D1 probe is shown in Fig. 7b for a $100kHz$ sampling rate in both the LES and experiment. The spectrum displays a dominant tone at an approximately $33kHz$ frequency in both the computation and experiment. The mechanism related to the genesis of this frequency will be explained further in Section 4. We summarize this section by reiterating that the simulations accurately reproduce the primary mean and unsteady features arising in this complicated flowfield.

3. Data Fusion

In Berry *et al.* (2017 PRoF), we exploit the superb accord between experiments and simulations to merge their strengths, thereby yielding an unprecedented level of integration. Specifically, within a POD framework, we fuse the superiorly statistically-converged experimental mode shapes with the high temporal-resolution LES database to enhance the time-resolution of the temporal coefficients within the POD. This is further explained within the context of Fig. 8, wherein we utilize an experimental and numerical Schlieren database sampled at $50kHz$ and $400kHz$ respectively. The most energetic flowfield feature, described in the first POD mode, is shown in Fig. 8(a), and is associated with periodic fluctuations within the three primary symmetry plane shear layers, along with regions outside of the jet. In fact, the frequency associated with these features has been shown to be consistent with the dominant $33kHz$ tone observed previously in the surface pressure spectra (Fig. 7(b)) (Stack & Gaitonde 2018 AIAAJ, Stack & Gaitonde 2018 AIAA). However, due to the $50kHz$ resolution of the experimental database, the proper $33kHz$ frequency is aliased to $15.7kHz$ as observed in Fig. 8(b). Nonetheless, when the fusion is performed, we obtain the proper temporal resolution of this mode as seen in Fig. 8(c). Thus, this novel methodology has enabled new fundamental physical insights, along with superior reduced-order models (*i.e.* POD) describing the primary unsteady features within this complex flowfield.

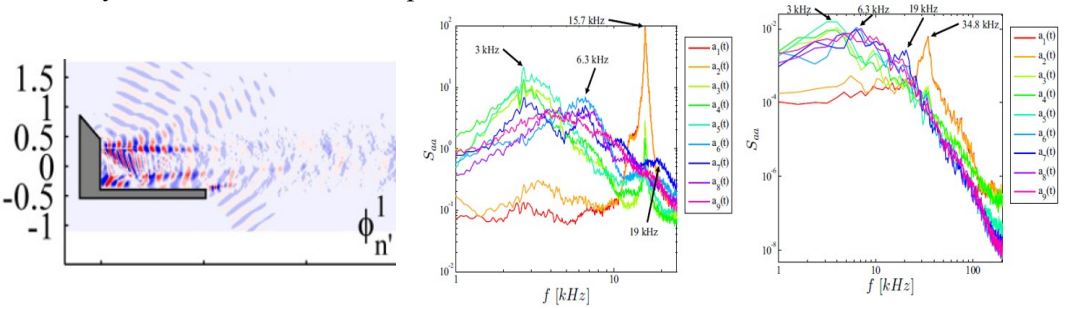

(a) The first spatial POD mode. (b) Experimental-only POD (c) Fused-POD spectra

Figure 8: **Results pertaining to the POD-based fusion of experimental and computational Schlieren data, (a) The first spatial POD mode from experiment, (b) Experimental-only POD and (c) fused-POD, note, not aliased in (c).**

4. Mean Flowfield

We now examine the dynamics of the mean flowfield, as obtained from time-averaging the LES data as well as some of the PIV data. Our focus is on the evolution and behavior of the various free and wall- bounded shear layers, the shock train, and the connection between the shock train and shear layer evolution, including the physical mechanism associated with the upwards plume deflection.

Figure 9a, essentially a zoomed-in version of Fig. 3c, displays the mean u-velocity field. Four primary shear layers may be identified as marked. The upper shear layer (USL) forms between the flow exiting the single-sided expansion and the ambient. The splitter plate shear layer (SPSL) begins at the splitter plate trailing edge, where the deck and core streams first interact, and the deck boundary layer (DBL) develops on the aft-deck. Downstream of the deck, the lower shear layer (LSL) forms between the bottom of the plume and the ambient.

The shock train will be described using time-averaged contours of $\mathbf{V} \cdot \nabla P$, as shown in Fig. 9b. This quantity takes on positive (dark) and negative (light) values in adverse and favorable pressure gradients respectively. Thus, it is useful in identifying compressions/shocks (positive values), and expansions (negative values) in regions where the velocity field and pressure gradients are not generally aligned with each other. The main elements of the shock train are initiated at the splitter plate trailing edge. An initial expansion fan is followed by a shock wave (Shock 1), to locally equalize the pressure of the core and deck streams. Shock 1 traverses the core stream and impinges on the upper ramp, inducing a shock-boundary layer interaction (SBLI) with the upper ramp boundary layer. This yields local features common to those described in SBLI literature (see for example Gaitonde (2015)), and result in a reflected shock (Shock 2A). The end of the expansion ramp yields another shock (Shock 2B) as the flow equalizes with the freestream. Shocks 2A and 2B cross the plume and impinge on the DBL, causing another SBLI (the local region where these shocks impinge on the deck will be referred to as the "drill", following the nomenclature of Kan *et al.* (2018)). These shocks reflect off the drill, and are redirected to the USL while undergoing a merging process (Shock 3). The next reflection from the USL is weaker, and influences the shock that originates at the end of the deck (Shock 4), where the flow again locally equalizes with the freestream. Further downstream, the shock train continues through repeated weaker reflections from the shear layers. For completeness, we note that other wave structures are generated

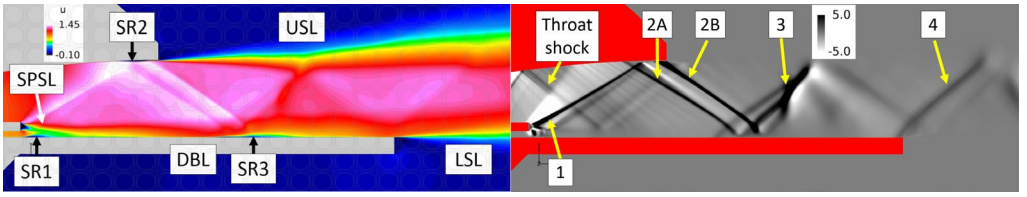

Figure 9: **Time-averaged symmetry plane contours of: (a) u-velocity, (b) $\mathbf{V} \cdot \nabla P$. USL=upper shear layer, SPSL=splitter plate shear layer, DBL=deck boundary layer, and LSL=lower shear layer. SR=separated region.**

in the interior of the nozzle, including a shock that originates at the nozzle throat (*i.e.* throat shock), and a series of weak compression waves along the SERN (not highlighted). Three primary separated regions are identified as marked in Fig. 9a. The first occurs in the DBL just downstream of the splitter plate trailing edge (SR1), which induces the wave pattern immediately downstream of Shock 1. The second (SR2) and third (SR3) separated regions occur near the respective ramp and drill SBLI regions, with each having a finite streamwise spatial extent. Of these, the drill separation (SR3) is highly three-dimensional due to the shock train three-dimensionality, which is described next.

The features of the shock train are setup by the combination of the SERN, rectangular cross-section, and presence of the aft-deck. To examine the shock train topology, we examine isosurfaces of $\mathbf{V} \cdot \nabla P = 0.2$ colored by the vertical distance from the deck (Fig. 10). As discussed previously in the context of Fig. 9b, the expansion ramp shocks (2A/2B) impinge on the DBL and are reflected as Shocks 3A/3B, while Shock 4 forms at the aft-deck trailing edge. At the nozzle exit, a shock emanates from each side-wall due to the slightly overexpanded conditions, thereby resulting in the observed diamond pattern. These side-wall shocks, which extend from the aft-deck surface to the SERN at the nozzle exit, gradually decrease in height moving inboard, as well as downstream, due to shear layer growth. Throughout the shock train evolution, the SERN-associated shocks (2A, 2B, 3A, 3B, 4) continually interact with the side-wall shocks and subsequent reflections, resulting in a complex three-dimensional flowfield, particularly on the DBL as discussed next.

To attain an understanding of the three-dimensional complexity of the DBL as a result of the shock train three-dimensionality, we utilize a simulated surface oil flow (also denoted surface streamlines) colored by pressure (Fig. 11). The nozzle geometry is translucent red to facilitate the visualization of streamlines from the end of the splitter plate. As discussed above, the first separated region (SR1) is observed just after the splitter plate trailing edge, as indicated by the coalescing streamlines. This separation is essentially two-dimensional, in that it extends across the span of the jet. The most prominent separation region occurs downstream of the nozzle exit, marked SR3 in Fig. 11, where Shocks 2A/2B interact with the DBL (the drill). This separation may be characterized in terms of lines of coalescence (separation) and divergence (attachment) (Perry & Fairlie 1974). The initial line of separation is marked S1, and the corresponding attachment is A1. For three-dimensional interactions, such as these, typically an open separation is obtained (*i.e.,* no closed recirculation bubble exists even in the mean flowfield, see also Schmisseur & Gaitonde (2001)). A second separation and attachment line pair (S2 and A2 respectively) is also evident, starting closer to the spanwise deck edge and extending inboard. This region of separated flow does not extend to the spanwise edges of the

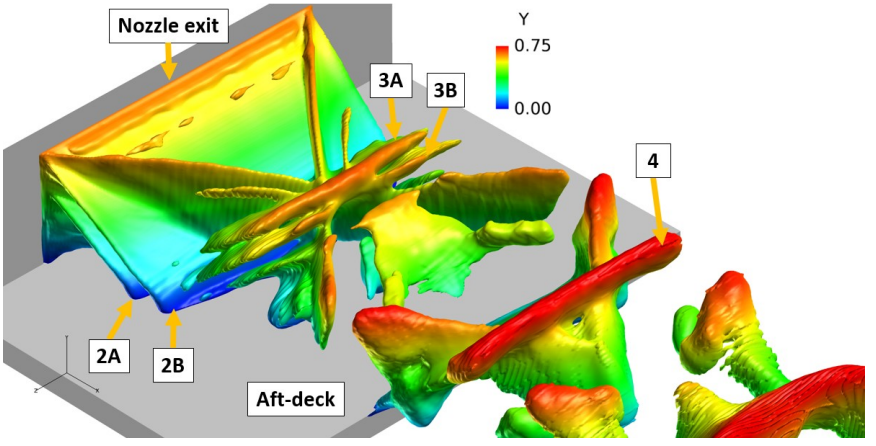

Figure 10: **Isosurfaces of $\mathbf{V} \cdot \nabla P = 0.2$ colored by the vertical distance from the aft-deck.**

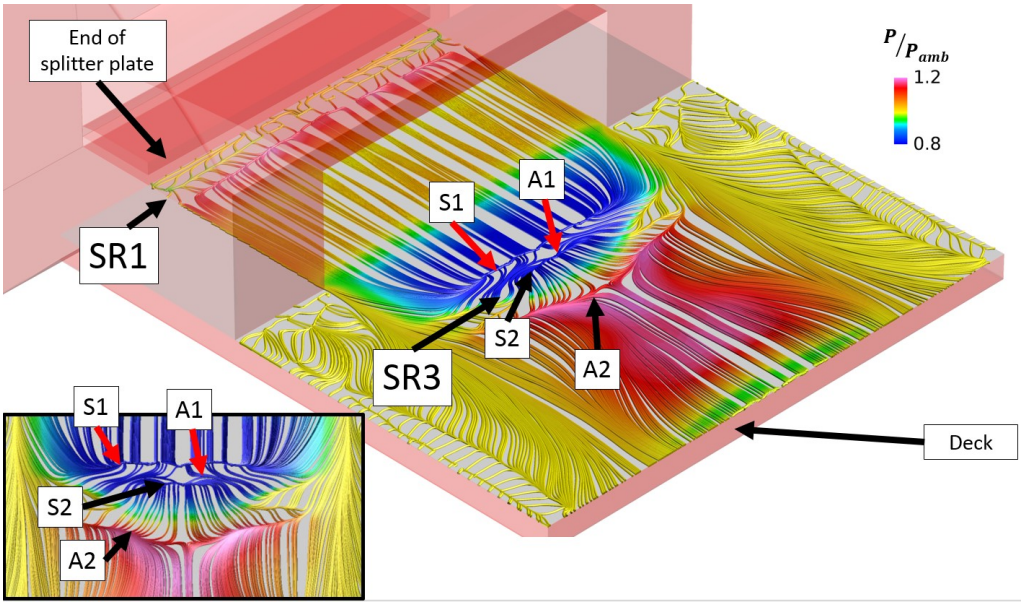

Figure 11: **Time-averaged simulated surface oil flow on the deck colored by pressure. The nozzle geometry is colored red, and is translucent to allow visualization of streamlines beginning at the splitter plate trailing edge. SR=separated region. The inset is a zoomed-in top-view of SR3 to better highlight the separation and attachment regions.**

deck because of the relief effect associated with the finite spanwise extent. Proceeding downstream, while also considering the *u*-velocity contours in Fig. 8a, the correlation between flow acceleration/deceleration and a favorable/adverse pressure gradient can be clearly discerned in this near-wall region.

We now discuss the development of the plume downstream of the nozzle components. Contours of the time-averaged *u*-velocity are shown in Fig. 12 at several streamwise locations from both experiment and simulation. Numerous features may be delineated. The anticipated shear layer growth

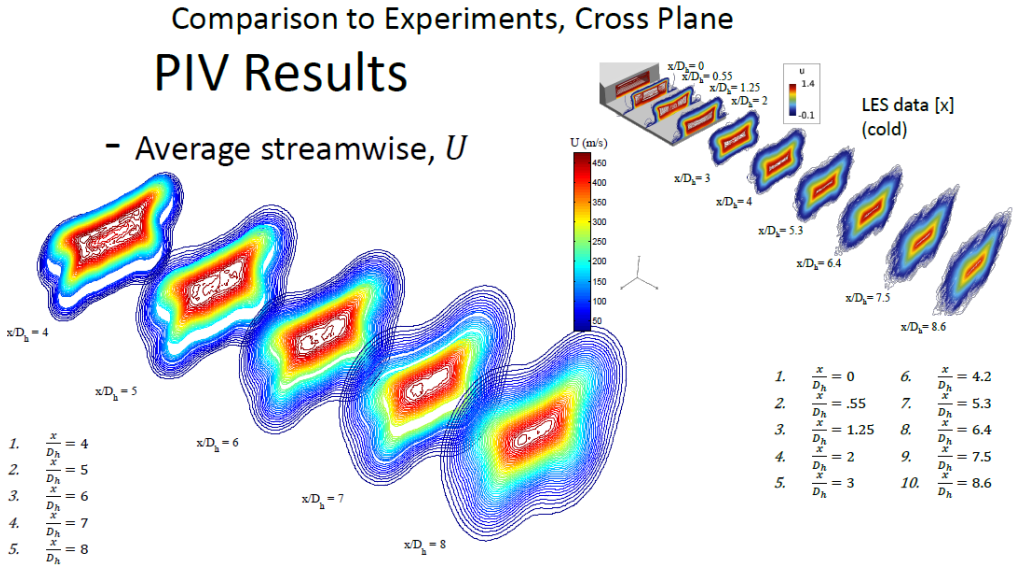

Figure 12: **Time-averaged contours of *u*-velocity at selected downstream locations, left from PIV, right from LES.**

resulting from entrainment of the ambient air is apparent, and furthermore, is asymmetric due to the fact that the aft-deck inhibits mixing with the ambient atmosphere. The most prominent feature is the gradual transition of the plume from a rectangular cross-section near the nozzle exit, to a more circular cross-section downstream. The corners play a significant role in these dynamics (Gutmark & Grinstein 1999), as evident in the distortion of the cross-sectional shapes in the corner regions. No axis switching is observed. In an experimental study on rectangular free jets, Zaman (1996) noted that axis switching is resisted if the pairs of counter-rotating vortices on the ends of the major axis are of the outflow-type (*i.e.,* with a rotation that tends to eject fluid from the plume into the ambient atmosphere).

As discussed earlier, there is an upwards vectoring of the plume downstream of the aft-deck trailing edge (see Fig. 3). This plume deflection has important ramifications on control systems, since although this phenomenon could be leveraged for thrust-vectoring purposes, there may be occasions when the system needs to compensate for the propulsion-induced moment on the vehicle. An understanding of the physical mechanism responsible for the plume deflection would allow the anticipation of when such phenomena may occur, and how severe it will be. For this, we supplemented the primary case above with two auxiliary simulations. The nominal mesh is employed for these, since it captures the shock train quite well, and reproduces changes in the plume deflection due to changes in the configuration, and/or stagnation conditions, without the need for prohibitive computational resources. In the first auxiliary simulation, hereafter referred to as AUX1, only the NPR_{core} is changed to NPR_{core}=5.5 (all other cases are NPR_{core}=4.65). For the second simulation, AUX2, the aft-deck length is decreased, with all remaining parameters identical to the primary case.

Results pertinent to the plume deflection from these simulations are shown in Fig. 13. For reference, Fig. 13a shows the shock and expansion locations from the primary case with time-averaged $\mathbf{V} \cdot \nabla P$ contours on the symmetry plane (similar to Fig. 9b). The time-averaged symmetry plane *u*-velocity field for AUX1, shown in Fig. 13b, exhibits a

modest downward plume deflection, with an estimated deflection angle of -0.92^o, while the plume in AUX2 (Fig. 13d) is effectively horizontal. These results show that the plume deflection for the configuration of this study can also be altered by the NPR and/or the aft-deck length (see also the discussion in Behrouzi & McGuirk (2015)).

The plume deflection may be connected to the shock train by examining the $\mathbf{V} \cdot \nabla P$ fields as before. Although the broad features are similar in many respects, including the presence and locations of the various shocks, several major differences may be identified between the primary and AUX1 case. First, the shock-cells are elongated for the AUX1 case. Elongated shock-cells for higher NPRs have been observed by Behrouzi & McGuirk (2015), who also reported a modification in the plume deflection angle with the NPR, which they attributed to the deck pressure distribution setup by the aft-deck shock train. Second, the shock induced by SR1 is much stronger for the AUX1 case than the primary and AUX2 cases, due to the larger separated region in the former. Third, only Shock 2A emanates from the expansion ramp in the AUX1 case (Shock 2B is absent due to pressure consistency at the nozzle exit from the separated expansion ramp boundary layer). Finally, the characteristics of the shock train differ at the aft-deck trailing edge between the cases. In the primary case, a shock is present at the deck-end to increase the fluid pressure to match that of the ambient, whereas the AUX1 case has an expansion fan at the deck-end to diminish the fluid pressure to match the ambient. The shock train features of the primary and AUX2 cases can be compared using Figs. 13a and 13e. As expected, the features are nearly identical before the deck-end, and differ only downstream of the deck.

The corresponding effects of the aft-deck shock train on deck pressure distributions are shown in Fig. 13f. Beginning with the primary case on the left, a large low pressure region is evident as the flow expands, and is followed by a large high pressure region downstream of the drill. The elongation of the shock cells in the AUX1 case (middle image) moves the low pressure region near the nozzle exit to the downstream half of the deck. The subsequent high pressure region also moves correspondingly further downstream and effectively off the deck. The deck pressure distributions for the primary and AUX2 cases can be compared using the left and rightmost images from Fig. 13f. As expected because of the similar aft-deck shock trains, the deck pressure distributions are nearly identical over the same aft-deck length. The only apparent difference is a reduced pressure magnitude near the deck-end of the AUX2 case compared to the same streamwise location for the primary case. This is consistent with a relief effect, as a portion of the high pressure region that was enclosed by the deck in the primary case is now exposed to the ambient in the AUX2 case.

Local conditions at the aft-deck trailing edge are thus clear indicators of the plume deflection characteristics. A comparison of the shock train features at the deck-end for the three cases reveals that a shock manifests in the primary case when the plume deflects upwards, an expansion fan occurs in the AUX1 case when the plume deflects downwards, and a weak expansion fan is present in the AUX2 case when the plume exhibits minimal deflection.

To further examine the connection of local conditions to the overall plume deflection, we consider oblique shock and Prandtl-Meyer function relations. Considering the primary case, the time-averaged Mach number is first extracted at the location marked with a red "x" in Fig. 13a (M~1.68), and the oblique shock angle is estimated to be β~40.37^o. Substituting these values into the θ-β-M relation, the deflection angle is estimated as θ~4.04^o, which is close to the plume deflection angle of 3.83^o noted previously. For the AUX1 case, the equivalent deck-end feature is an expansion. By evaluating the Prandtl-Meyer function with time-averaged Mach numbers upstream and downstream of the expansion fan at the locations marked with a red "x" in Fig. 13c, the turn angle may

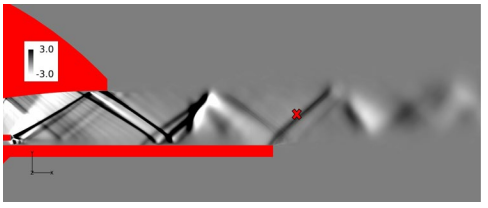

(a) Primary time-averaged symmetry plane $\mathbf{V} \cdot \nabla P$.

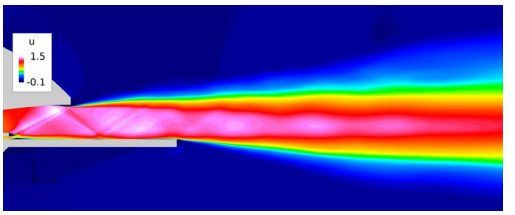

(b) AUX1 time-averaged symmetry plane u-velocity.

(c) AUX1 time-averaged symmetry plane $\mathbf{V} \cdot \nabla P$.

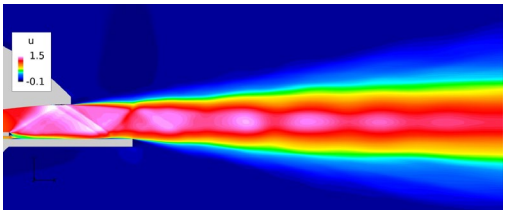

(d) AUX2 time-averaged symmetry plane u-velocity.

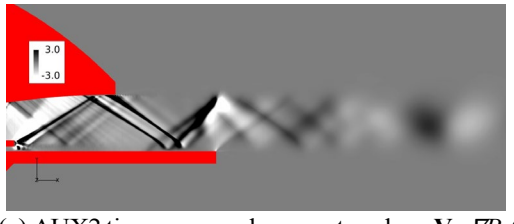

(e) AUX2 time-averaged symmetry plane $\mathbf{V} \cdot \nabla P$.

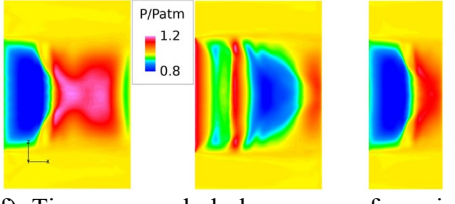

(f) Time-averaged deck pressure for primary (left), AUX1 (center), and AUX2 (right) cases. The left side is the nozzle exit and the right side is the deck-end.

Figure 13: **Impact of nozzle conditions and geometry on the plume development with time-averaged shock structure, u-velocity, and deck pressure.**

be estimated as $\theta \sim -1.02^o$, which approximates the downward plume deflection angle of -0.92^o noted earlier. A similar analysis cannot be performed for the AUX2 case, since there is no dominant shock/expansion across the core of the plume that emanates from the deck-end. These results demonstrate that by carefully specifying the operating conditions of the jet (NPR), and/or the aft-deck length, the aft-deck pressure characteristics can be adjusted to influence the nature of the shock train at the deck-end and subsequent plume deflection, leading to possible control opportunities through thrust-vectoring.

5. Unsteady Flowfield

The primary unsteady characteristics of the flowfield are now discussed using statistics and instantaneous realizations. We begin by examining regions of substantial turbulence activity with mean turbulent kinetic energy (TKE) on the symmetry and several stream-wise planes. We then emphasize a shedding instability at the splitter plate trailing edge,

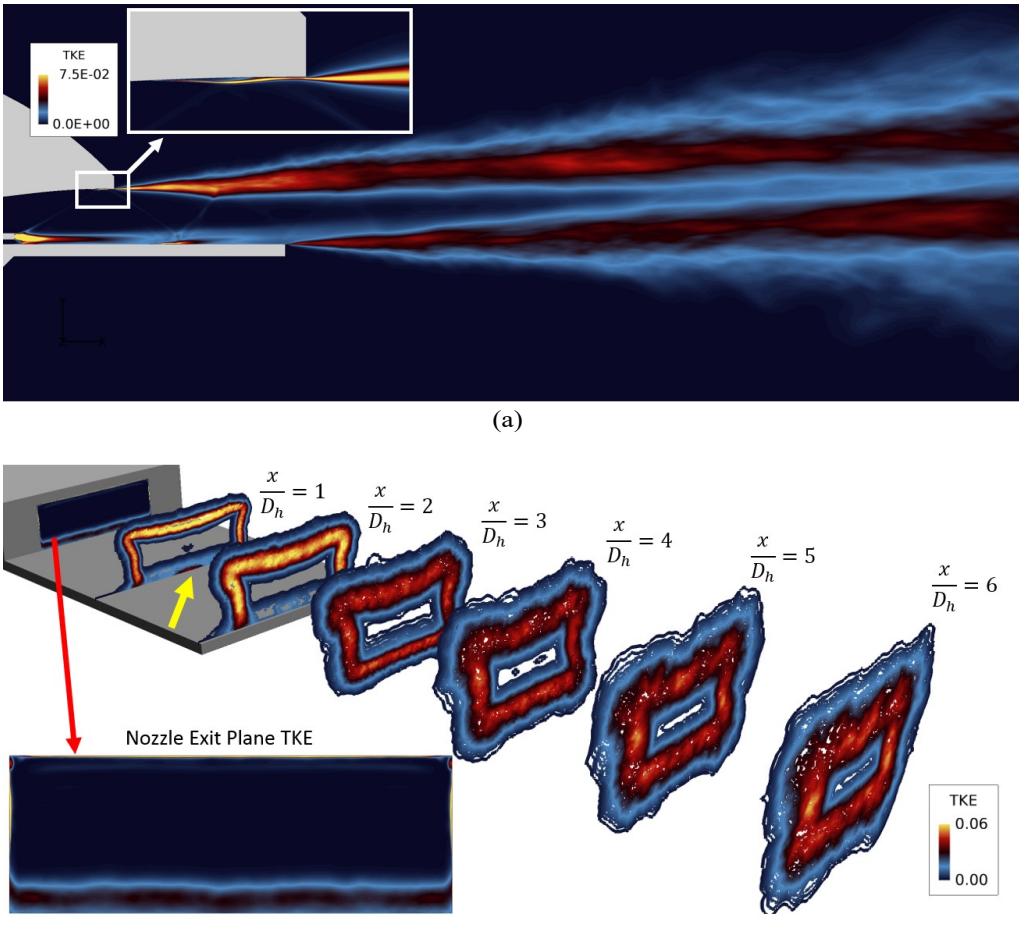

Figure 14: **Contours of mean turbulent kinetic energy: a) on the nozzle symmetry plane, b) at selected streamwise locations.**

which has implications on the entire flowfield, including the shock train and the tone observed earlier in Fig. 8b.

As a representative of the turbulence field, time-averaged TKE contours are shown at the nozzle symmetry plane and several streamwise locations in Fig. 14. High levels of TKE are evident in several regions along the symmetry plane (Fig. 14a). The largest TKE region occurs in the SPSL, indicating significant unsteadiness in the shear layer between the core and deck streams. The USL also depicts substantial levels of TKE near the edge of the expansion-ramp, where the fluid reaches its maximum velocity, and the relative shear with the ambient is large. Other regions of high TKE are observed near the drill and the separated region on the upper ramp as a result of the previously-described SBLIs, consistent with the discussion of Smits & Muck (1987) on increased turbulence due to SBLI.

Crossflow planes of TKE are shown in Fig. 14b. At the nozzle exit plane, high levels of TKE are localized in the boundary layers, particularly on the upper ramp boundary layer, upper corner regions, and side-wall boundary layers. Further downstream, high values of TKE occur primarily along the regions of the plume exposed to the ambient, along with

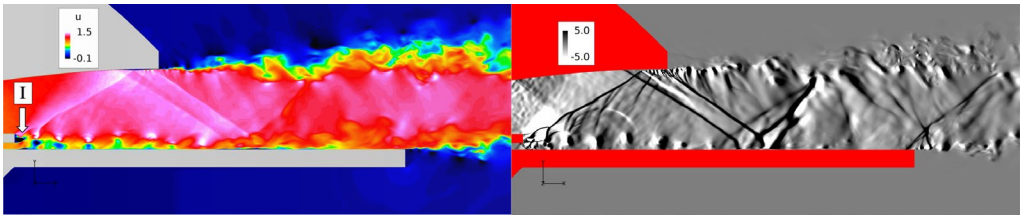

(a) (b)

Figure 15: **Instantaneous symmetry plane visualizations of the flow: a) u- velocity, b) $\mathbf{V} \cdot \nabla P$. The arrow marked "I" highlights the location of the shedding instability at the splitter plate trailing edge.**

a small concentrated region on the symmetry plane near the deck, as highlighted by the yellow arrow. The finite span of this highly-unsteady region is another manifestation of the three-dimensional nature of the shock train. It was shown earlier (Figs. 6 and 10) that the shocks emanating from the side walls interact with each other slightly downstream of the drill at the nozzle symmetry plane. Thus along the symmetry plane, the DBL interacts not only with the Shocks 2A/2B, but also with the coalescing side wall shocks. As the plume continues to develop downstream, peak turbulent fluctuations diminish and the high TKE regions spread towards the center of the major and minor axes. At the same time, the plume gradually transforms from a rectangular cross-section to a more axisymmetric cross-section, as previously discussed.

To highlight other important aspects of the instantaneous flowfield, contours of u-velocity and $\mathbf{V} \cdot \nabla P$ are shown in Fig. 15; these are the counterparts of the mean flow data of Fig. 9. Numerous features are evident from the u-velocity in Fig. 15a. First, at the splitter plate trailing edge, a shedding instability is observed, initiated in the region marked "I". These periodic structures gradually diminish downstream as they are damped by the DBL. Fine scale unsteadiness is also generated at each SBLI discussed previously in the context of Figs. 9a and 14b. Manifestations of unsteadiness can also be observed in the pressure field (Fig. 15b). The perturbations associated with the shedding process propagate along Shock 1 (see Fig. 9b for nomenclature) and continue along Shocks 2A/2B. As such, the signature of the shedding can be observed in the region near the lip of the expansion ramp as well as the drill region, as will be shown later. The structures formed by the shedding in the SPSL are also visible, where each pair of black and white contours represent a single structure. Finally at the aft-deck trailing edge, the distortion of Shock 4 further indicates the high levels of unsteadiness associated with the shock train.

As discussed in Section 2, a dominant tone at $33kHz$ is observed in both computational and experimental deck pressure spectra. This tone is closely related to the shedding instability occurring at the end of the splitter plate. The signal at a point probe placed downstream of the shedding (Fig. 16a) was analyzed to determine the frequencies associated with the shedding. Data were sampled every time-step (roughly a $21MHz$ sampling rate) for 683,000 time-steps, corresponding to about $32.3ms$ of physical time. Spectral analyses were performed on both pressure and u-velocity signals as shown in Fig. 16b. The PPSD highlights three main frequencies, namely $33kHz$ and its harmonics, $66kHz$, and $99kHz$. An small fourth peak ($132kHz$) is also observed, but primarily in the u-velocity spectrum. It can be reasoned therefore that the instability between the streams is related to the dominant $33kHz$ tone. The harmonics can be associated with

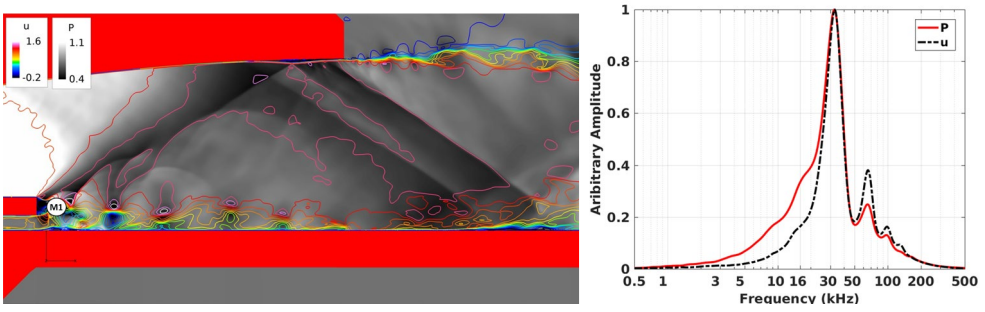

(a) Location of the point probe. Solid contours are pressure, and contour lines are u-velocity.

(b)

Figure 16: **Unsteady content of the M1 probe: (a) probe location, (b) PPSD of pressure and u-velocity.**

non-linear mechanisms that arise when the shed structures break down as they evolve in the presence of the SPSL and the DBL.

To highlight how this tone pervades the domain, space-time correlations are performed on the symmetry plane pressure field using 2000 snapshots sampled at roughly $405kHz$. The M1 probe is considered the reference location, and its signal is band-pass filtered around the tone frequency ($33kHz$). The band-pass filtered signal is then correlated with the raw signals in the remainder of the domain.

The result from the above procedure at zero lag is shown in Fig. 17, where each alternating positive-negative correlation peak represents one period of an event. Large-scale pressure waves are readily apparent in the acoustic region outside the plume, whose origin can be traced to the splitter plate trailing edge where shedding is initiated. Although the correlation magnitude decreases with increasing distance from the splitter plate, these waves clearly exhibit a far-field signature, consistent with the noise spectra of Berry *et al.* (2016). Additionally, small-scale periodic structures, highlighted by dashed boxes, are interspersed with the large-scale waves.

Before describing the connection between the large-scale waves and small-scale periodic structures, several other observations can be made regarding Fig. 17. First, the black arrow near the splitter plate trailing edge highlights alternating peaks near the upper and lower halves of the plate, indicating the pressure fluctuations are out-of-phase, consistent with the oscillating center of pressure in the wake of a shedding body. Additionally, as discussed above, Shock 1 is continually perturbed by the shedding, and the alternating peaks along Shock 1 provide evidence that these perturbations persist to the upper ramp, in turn influencing the SBLI and USL development. Lastly, alternating peaks are also present inside the dashed box in the SPSL, and represent the convection of the low pressure vortex cores generated by the shedding (Figs. 15 and 16a).

The connection between the small-scale periodic structures and the large-scale waves is established by considering the propagation path of a wavefront in different directions. The discussion is divided into the wavefront to the left and right of the angled dashed arrow, as well as along the downstream direction, as shown by the horizontal dashed arrow. The wavefront to the left of the angled dashed arrow propagates until it interacts with the expansion ramp surface upstream of the nozzle lip, generating two effects on the downstream flowfield. The first effect is to influence the growth of structures near the SBLI/USL region. The periodic excitation of this region due to the incident wavefront

results in the periodic small-scale structures inside the dashed box in the USL, which are interspersed with the large-scale peaks from the waves. Additional evidence for the influence of these waves on the USL growth can be found in the analysis of Berry *et al.* (2017), and the instantaneous experimental Schlieren (Fig. 5b), where the several distinct black regions (representative of fluid structures) beneath the yellow arrow have a similar spacing as the small correlation peaks inside the dashed box. Traces of these structures vanish further downstream in both the experimental Schlieren, as well as the correlation analysis, due to the influence of turbulence in the USL. The second effect of the incident wave/expansion ramp interaction is the redirection of the wave along Shocks 2A/2B, as indicated by the alternating peaks along these shocks. Although the correlation magnitudes along the shocks are smaller than the wavefronts themselves, the results demonstrate the manner in which the tone is redirected through the domain by the shock system.

The transverse-propagating wave to the right of the angled dashed arrow is connected to the radiation observed above the nozzle in Fig. 17. The portion that propagates directly along the angled dashed arrow is diffracted around the nozzle lip to produce the radiation evident in the upstream/transverse directions. Meanwhile, the transverse-propagating portions to the right of the angled dashed arrow maintain their initial propagation path to result in the radiation apparent in the transverse/downstream directions.

The portions of a wave that propagate primarily in the streamwise direction (the direction of the horizontal dashed arrow) experience differences between the USL and DBL sides. As discussed above, the USL turbulence modulates the waves, thus they are absent in the USL downstream of the deck. However, as evident by comparing the correlation magnitudes of a given wave above and below the horizontal dashed arrow, it is clear that waves near the DBL exhibit higher correlations, and remain coherent much further downstream due to the presence of the wall. Eventually, the wavefront near the DBL is diffracted at the aft-deck trailing edge to generate the radiation evident below the nozzle. Additionally, these waves periodically excite the LSL as indicated by the small-scale periodic structures inside the dashed box at the aft-deck trailing edge. Such structures have also been observed in the experimental analysis of Berry *et al.* (2017). This correlation analysis clearly demonstrates how the unsteadiness initiated by the shedding influences the flowfield, namely the USL/LSL evolution, and the generation of the primary tone observed in the deck pressure (Fig. 7).

A detailed analysis of the signal pathways that ultimately project the signature of this tone into the domain has been outlined in Kan et al. (2018). Using conventional Fourier band-pass as well as wavelet filters, we have gained operational experience with the mapping of propagation pathways, by cross-correlating the entire field with a judiciously selected reference signal. The frequency-dependence of these pathways point to distinct physics associated with specific pathways. The information about the propagation of fluctuations in the near jet and its vicinity, obtained from frequency-specific cross-correlations, is summarized in Fig. 18.

While acoustic and/or convective propagation in the core flow and along shear layers is consistent with familiar mechanisms, the role of oblique shocks as wave guides was not previously studied. It was qualitatively confirmed by time-resolved Schlieren observations as part of this study. Attempts to establish an analytical foundation for this observation are still in progress.

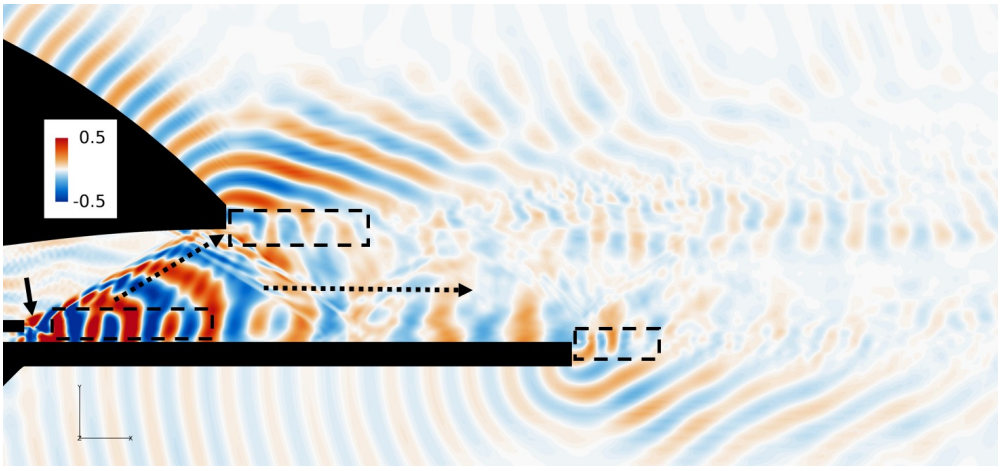

Figure 17: **Symmetry plane space-time correlation of pressure at zero lag using the band-passed M1 probe as the reference signal. The nozzle geometry is colored black.**

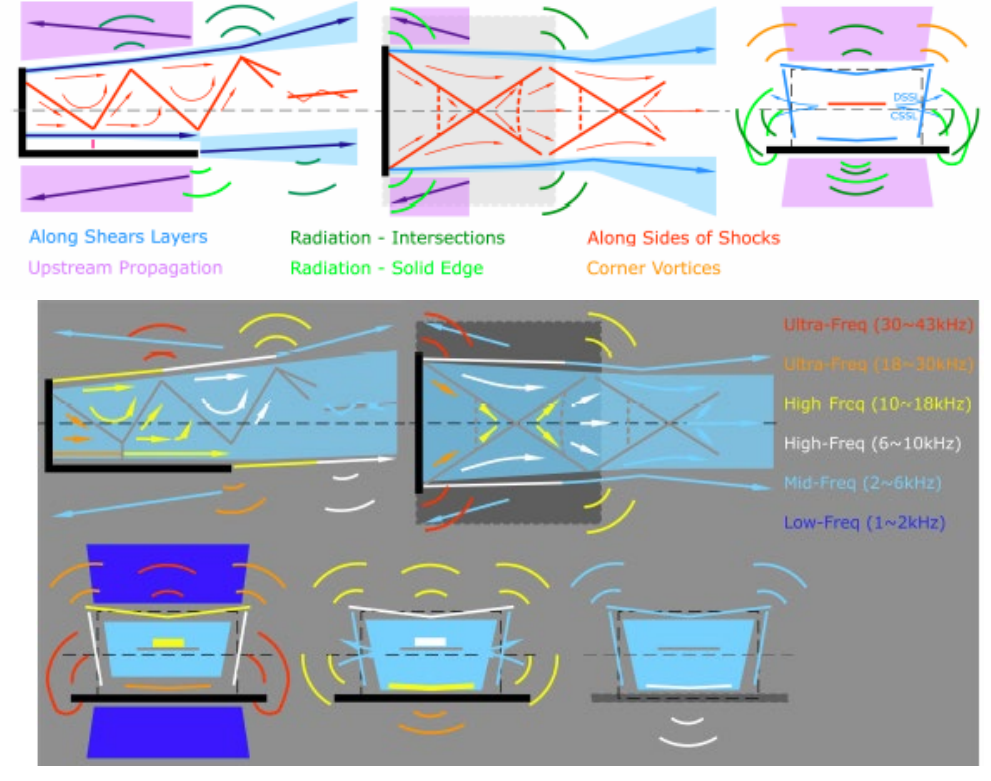

Figure 18: **Propagation pathways in the near jet.**

6. Summary

This experimental and simulation effort was carried with very close collaboration between the two. The primary technique employed for the simulations comprised Large-Eddy Simulations at the full Reynolds number of the experiment and the experiments where performed with PIV, unsteady pressure and time-dependent Schlerien. The validations showed great agreement between the simulations and experiments for the primary mean and unsteady features observed. Based on this agreement, the simulations were used for two purposes, 1) for a novel data fusion with the experiments and 2) probed to yield a detailed understanding of i) the multiple free and bounded shear layers occurring in the flowfield, ii) the three-dimensional nature of the shock train, and a iii) the connection between the shock train and the various shear layers; namely the relation between the shock train and the behavior of the aft-deck boundary layer, as well as the link between the plume deflection, aft-deck pressure field, and the shock train. Through the combination of instantaneous realizations of the flowfield, spectral analyses of both simulation and experimental data, and carefully-tailored space-time correlations, the genesis of the primary tone observed in the deck pressure spectra, and far-field experimental noise spectra, to a shedding instability occurring at the trailing edge of the splitter plate that divides the two streams. Using conventional Fourier band-pass as well as wavelet filters, we have gained operational experience with the mapping of propagation pathways, by cross-correlating the entire field with a judiciously selected reference signal. The frequency-dependence of these pathways point to distinct physics associated with specific pathways.

REFERENCES

Adler, M. & Gaitonde, D. V. 2017 Unsteadiness in swept-compression-ramp shock/turbulent-boundary-layer interactions. *55th AIAA Aerospace Sciences Meeting, AIAA Paper 2017-0987*.

Adler, M. C., Gonzalez, D. R., Stack, C. M. & Gaitonde, D. V. 2018 Synthetic generation of equilibrium boundary layer turbulence from modeled statistics. *Computers and Fluids* **165**, 127–143.

Beam, R. & Warming, R. 1978 An implicit factored scheme for the compressible navier-stokes equations. *AIAA Journal* **16** (4), 393–402.

Behrouzi, P. & McGuirk, J. 2015 Underexpanded jet development from a rectangular nozzle with aft-deck. *AIAA Journal* **53** (5), 1287–1298.

Berry, M.G., Magstadt, A.S., Glauser, M.N., Ruscher, C.J., Gogineni, S. & Kiel, B.V. 2016 An acoustic investigation of a supersonic, multi-stream jet with aft deck: Characterization and acoustically-optimal operating conditions. In *54th AIAA Aerospace Sciences Meeting, AIAA Paper 2016-1639*.

Berry, M. G., Magstadt, A. S. & Glauser, M. N. 2017 Application of pod on time-resolved schlieren in supersonic multi-stream rectangular jets. *Physics of Fluids* **29**, 020706.

Berry, M.G., Stack, C.M., Magstadt, A.S., Ali, M.Y., Gaitonde, D.V. and Glauser, M.N., 2017 Low-dimensional and data fusion techniques applied to a supersonic multistream single expansion ramp nozzle, *Physical Review of Fluids* **2**, 100504

Bogey, C. & Bailly, C. 2010 Influence of nozzle-exit boundary-layer conditions on the flow and acoustic fields of initially laminar jets. *Journal of Fluid Mechanics* **663**, 507–538.

Dhamankar, N. S., Martha, G. S., Situ, Y., Aikens, K. M., Blaisdell, G. A., Lyrintzis, A. S. & Li, Z. 2014 Digital filter-based turbulent inflow generation for jet aeroacoustics on non-uniform structured grids. *52nd AIAA Aerospace Sciences Meeting, AIAA Paper 2014-1401*.

Gaitonde, D.V. & Samimy, M. 2011 Coherent structures in plasma-actuator controlled supersonic jets: Axisymmetric and mixed azimuthal modes. *Physics of Fluids* **23** (9).

Gaitonde, D.V. & Visbal, M.R. 1998 High-Order Schemes for Navier-Stokes Equations: Algorithm and Implementation into FDL3DI. *Tech. Rep.* AFRL-VA-WP-TR-1998-3060. Air Force Research Laboratory, Wright-Patterson AFB.

Gaitonde, D. V. 2015 Progress in shock-wave boundary layer interactions. *Progress in Aerospace Sciences* **72**, 80–99.

Gonzalez, D. R., Speth, R. L., Gaitonde, D. V. & Lewis, M. J. 2016 Finite-time lyapunov exponent-based analysis for compressible flows. *Chaos: An Interdisciplinary Journal of Nonlinear Science* **26**, 083112.

Grinstein, F.F., Margolin, L.G. & Rider, W.J. 2007 *Implicit Large Eddy Simulation, Computing Turbulent Fluid Dynamics*. Cambridge Univ Press.

Gutmark, E. J. & Grinstein, F. F. 1999 Flow control with noncircular jets. *Annual Review of Fluid Mechanics* **31**, 239–272.

Kan, P., Ruscher, C. J., Lewalle, J. & Gogineni, S. 2018 Near-field shock/shear-layer interactions in a two-stream supersonic rectangular jet from three-stream engine. *AIAA Journal* **56** (3), 1031–1046.

Klein, M., Sadiki, A. & Janicka, J. 2003 A digital filter based generation of inflow data for spatially developing direct numerical or large eddy simulations. *Journal of Computational Physics* **186**, 652–665.

van Leer, B. 1979 Towards the ultimate conservative difference scheme. v. a second-order sequel to godunov's method. *Journal of Computational Physics* **32**, 101–136.

Magstadt, A.S., Berry, M.G., Coleman, T.J., Shea, P.R., Glauser, M.N., Ruscher, C.J., Gogineni, S. & Kiel, B.V. 2016 A near-field investigation of a supersonic, multi-stream jet: locating turbulence mechanisms through velocity and density measurements. In *54th AIAA Aerospace Sciences Meeting, AIAA Paper 2016-1639*.

Magstadt, A. S. 2017 Investigating the structures of turbulence in a multi-stream, rectangular, supersonic jet. PhD thesis, Syracuse University.

Papamoschou, D. & Debiasi, M. 2001 Directional suppression of noise from a high speed jet. *AIAA Journal* **39** (3), 388–395.

Perry, A.E. & Fairlie, B.D. 1974 Critical Points in Flow Patterns. *Advances in Geophysics* **18B** (299-315).

Roe, P.L. 1981 Approximate reimann solvers, parameter vectors and difference schemes. *Journal of Computational Physics* **43**, 357–372.

Schmisseur, J.D. & Gaitonde, D.V. 2001 Numerical investigation of strong crossing shock-wave/turbulent boundary-layer interactions. *AIAA Journal* **39** (9), 1742–1749.

Smits, A.J. & Muck, K-C. 1987 Experimental study of three shock wave/turbulent boundary layer interactions. *Journal of Fluid Mechanics* **182**, 291–314.

Speth, Rachelle & Gaitonde, D. 2012 The effect of laminar nozzle exit boundary layer thickness on a mach 1.3 jet with and without control. *42nd AIAA Fluid Dynamics Conference and Exhibit, AIAA Paper 2012-2691*.

Speth, R. L. & Gaitonde, D. V. 2015 Nozzle-exit boundary-layer effects on a controlled supersonic jet. *AIAA Journal* **53**, 2027–2039.

Stack, C. M. & Gaitonde, D. V. 2017 Unsteady features in a rectangular supersonic multistream jet with and aft-deck. In *55th AIAA Aerospace Sciences Meeting, AIAA Paper 2017-0557*.

Stack, C. M. & Gaitonde, D. V. 2018 Shear layer dynamics in a supersonic rectangular multistream nozzle with an aft-deck. *AIAAJ*.

Touber, E. & Sandham, N. D. 2008 Oblique shock impinging on a turbulent boundary layer: Low-frequency mechanisms. In *38th Fluid Dynamics Conference and Exhibit, AIAA Paper 2008-4170*

Vinokur, M. 1974 Conservation Equations of Gasdynamics in Curvilinear Coordinate Systems. *Journal of Computational Physics* **14**, 105–125.

Visbal, M.R. & Gaitonde, D.V. 1997 Implementation of a High-Order Accurate Finite-Difference Scheme for DNS/LES. In *Proceedings of the First AFOSR International Conference on DNS/LES*. Louisiana Tech Univ., Ruston, LA.

Visbal, M. & Gaitonde, D. 2001 Very high-order spatially implicit schemes for computational acoustics on curvilinear meshes. *J. Comp. Acoustics* **9** (4), 1259–1286.

Zaman, K. B. M. Q. 1996 Axis switching and spreading of an asymmetric jet: the role of coherent structure dynamics. *Journal of Fluid Mechanics* **316**, 1–27.

Zaman, K. M. B. Q. 2012 Effect of initial boundary-layer state on subsonic jet noise. *AIAA Journal* **50** (8), 1784–1795.